nature photonics

ARTICLES

https://doi.org/10.1038/s41566-018-0109-4

Combined multi-plane phase retrieval and super-resolution optical fluctuation imaging for 4D cell microscopy

A. Descloux[1,6], K. S. Grußmayer[1,6], E. Bostan[2,4], T. Lukes[1], A. Bouwens[1], A. Sharipov[1], S. Geissbuehler[1], A.-L. Mahul-Mellier[3], H. A. Lashuel[3], M. Leutenegger[1,5] and T. Lasser[1*]

Super-resolution fluorescence microscopy provides unprecedented insight into cellular and subcellular structures. However, going 'beyond the diffraction barrier' comes at a price, since most far-field super-resolution imaging techniques trade temporal for spatial super-resolution. We propose the combination of a novel label-free white light quantitative phase imaging with fluorescence to provide high-speed imaging and spatial super-resolution. The non-iterative phase retrieval relies on the acquisition of single images at each *z*-location and thus enables straightforward 3D phase imaging using a classical microscope. We realized multi-plane imaging using a customized prism for the simultaneous acquisition of eight planes. This allowed us to not only image live cells in 3D at up to 200 Hz, but also to integrate fluorescence super-resolution optical fluctuation imaging within the same optical instrument. The 4D microscope platform unifies the sensitivity and high temporal resolution of phase imaging with the specificity and high spatial resolution of fluorescence microscopy.

During the past two decades novel wide-field fluorescence imaging techniques (such as (d)STORM and PALM)[1–6] based on the localization of a stochastically activated subset of single molecules overcame the diffraction limit and provided new insights into subcellular structures. These techniques require long image sequences containing at least several hundred raw images. Therefore, the gain in spatial resolution comes at the cost of reduced time resolution[7]. Super-resolution optical fluctuation imaging (SOFI)[8,9] provides an elegant alternative for super-resolution imaging using higher-order cumulant statistics. SOFI is well suited for 3D live cell imaging with a moderate time resolution of up to ~1 second per reconstructed image in a multi-plane microscope[10]. In addition, SOFI tolerates high labelling densities[11,12] and can provide a quantitative assessment of molecular parameters[13,14].

Many biological processes, for example, membrane blebbing, neuronal signalling or cardiovascular cell dynamics, take place on a sub-second to sub-millisecond timescale[15,16]. As investigation of cell physiology demands long-term, fast imaging potentially unattainable for single-molecule localization microscopy[17], a novel imaging concept is needed. Our Phase Retrieval Instrument with Super-resolution Microscopy (PRISM) satisfies these needs as a versatile multi-plane platform with high image acquisition rates, integrating 3D fluorescence microscopy and a novel approach for white-light 3D phase retrieval. It enables multimodal 4D imaging, combining the molecular specificity and spatial resolution of fluorescence super-resolution with the sensitivity and high speed of quantitative phase imaging.

Phase imaging is a label-free approach, enabling long-term time-lapse imaging of cellular dynamics. In 1969, E. Wolf proposed a solution how to infer the refractive index distribution—that is, cell morphology—from scattered light acquisitions[18]. This seminal work launched a new field known as quantitative phase imaging (QPI), which aims at determining the optical phase delay induced by the refractive index distribution. The phase differences can be assessed with various techniques[19], such as measurement of the interference of the scattered field with a reference field (off-axis holography, HPM)[20–23], controlled phase-shift of the reference field (FPM, SLIM)[24,25] or by measuring defocused image planes (TIE)[26–29]. Several QPI concepts have been extended towards 3D live cell imaging[30–32], where the phase tomogram is acquired by *z*-scanning the sample or through successive projection measurements with multiple illumination angles[33].

In the present work, we retrieve the 3D quantitative phase from a stack of bright-field images using a simple Fourier filtering. We explain this white-light depth-resolved phase imaging based on the theory of 3D partially coherent image formation. The broad versatility of our technique is demonstrated by a number of cell images. We first extract the high-resolution 3D phase information of fixed cells from a large stack of *z*-displaced intensities. We then present PRISM, a multi-plane microscope for the simultaneous acquisition of eight planes. This novel configuration was used for monitoring cell dynamics at up to 200 Hz. Finally, we sequentially image cell samples with 3D SOFI and phase microscopy.

PRISM is conceived as an add-on to existing wide-field microscopes, enabling straightforward implementation of fast, 3D quantitative phase and 3D fluorescence super-resolution imaging, overall presenting a unique opportunity to study the complex spatial and temporal physiology of live cells.

[1]École Polytechnique Fédérale de Lausanne, Laboratoire d'Optique Biomédicale, Lausanne, Switzerland. [2]École Polytechnique Fédérale de Lausanne, Biomedical Imaging Group, Lausanne, Switzerland. [3]École Polytechnique Fédérale de Lausanne, Laboratory of Molecular and Chemical Biology of Neurodegeneration, Brain Mind Institute, Lausanne, Switzerland. [4]Present address: University of California, Berkeley, Computational Imaging Lab, Berkeley, CA, USA. [5]Present address: Max-Planck Institute for Biophysical Chemistry, Department of NanoBiophotonics, Göttingen, Germany. [6]These authors contributed equally: A. Descloux and K. S. Grußmayer. *e-mail: theo.lasser@epfl.ch

Results

3D white light partially coherent image formation. E. Wolf's solution[18] of the inverse light scattering problem is based on the Helmholtz wave equation and a Green's function ansatz which we used as the underlying theoretical framework for our tomographic 3D phase retrieval. The interaction between a plane wave $U_i(\mathbf{x};\omega,\mathbf{k}_i)$ and a weakly scattering object induces a scattered field $U_s(\mathbf{x};\omega,\mathbf{k}_i,\mathbf{k})$ which encodes the object's scattering potential $F(\mathbf{x})$ (Fig. 1a). Throughout the text, we use the short-hand notation $\mathbf{x} = (x,y,z)$ for cartesian coordinate, $\mathbf{g} = (g_\perp, g_z)$ for Fourier space. The frequency of the illumination and scattered field is denoted ω, the illumination wavevector $\mathbf{k}_i$ and the scattered wavevector $\mathbf{k}$. The illumination field is decomposed into plane wave components and fully characterized by its angular spectrum. Assuming a single plane wave and supposing weak elastic light scattering (using the first-order Born approximation[34]), we obtain an adequate model for the light–object interaction (see Supplementary Section 1.1). Taking into account the polychromatic illumination with its spectrum $S(\omega)$, we embedded our analysis in the framework of the generalized Wiener–Khintchine theorem[35]. Accordingly, we acquire an intensity encoding the interference of the scattered field with the illumination field (Fig. 1a). This results in a linear relation

$$\Gamma(\mathbf{g}) = iF(\mathbf{g})H(\mathbf{g}) \tag{1}$$

showing that the cross-spectral density[35] $\Gamma(\mathbf{g})$ is given as the product of the scattering potential $F(\mathbf{g})$ and the 3D partially coherent transfer function $H(\boldsymbol{g})$ in Fourier space (for the full derivation including underlying approximations, see Supplementary Section 1.2).

Based on the Ewald sphere construction, this complex interaction is illustrated in Fig. 1b, allowing an intuitive interpretation of elastic light scattering. For each source wavelength λ, the frequency support corresponds to a shifted sphere cap of radius $k_0 = \overline{n}\frac{2\pi}{\lambda}$, where $\overline{n}$ is the mean refractive index of the sample. The lateral spatial frequencies extend up to the frequency $g_{\perp,\max} = k_0(\mathrm{NA}_{\mathrm{ill}} + \mathrm{NA}_{\mathrm{det}})$ and depend on the numerical aperture of the Koehler illumination ($\mathrm{NA}_{\mathrm{ill}}$) and the detection objective ($\mathrm{NA}_{\mathrm{det}}$). The final transfer function takes into account the full temporal and angular illumination spectrum (see Supplementary Section 1.2, Supplementary Fig. 1).

Finally, we separate the 3D intensity $I(\mathbf{g})$ as the sum of a d.c.-component and an a.c.-component, where the a.c.-component contains the cross-spectral density $\Gamma(\mathbf{g})$ and its complex conjugate (Fig. 1c, Supplementary Section 2)

$$I(\mathbf{g}) \approx I_0\delta(\mathbf{g}) + \Gamma(\mathbf{g}) + \Gamma^*(-\mathbf{g}). \tag{2}$$

3D phase retrieval. The experimental procedure is straightforward and consists of acquiring N z-displaced intensities $I(x,y,z_p)$. The bright-field image stack encodes the 3D scattering potential as the interference between the scattered field and the incident field. Referring to the Ewald sphere (Fig. 1b), the attainable frequency support is restricted by the illumination and detection aperture and the illumination spectrum.

Using a low illumination $\mathrm{NA}_{\mathrm{ill}}$ ($\mathrm{NA}_{\mathrm{ill}} \leq 0.26$), the cross-spectral density is mainly contained in the upper half Fourier space (see Fig. 1b,c)[36,37]. As indicated in Fig. 2a, the cutoff filter $K(g_z) = \begin{cases} 1 & g_z > g_{z,c} \\ 0 & \text{else} \end{cases}$ selects $\Gamma_+(\mathbf{g}) = I(\mathbf{g})K(g_z)$ from the Fourier transformed intensity stack. The cutoff frequency $g_{z,c}$ is determined by the source spectrum and the illumination aperture (see Supplementary Section 2). This filtering implies several far-reaching consequences. First, the cutoff filter allows one to select the complex cross-spectral density $\Gamma_+(\mathbf{g})$. Second, $K(g_z)$ suppresses the spectral overlap occurring at low axial frequencies. A simple estimation of the consequences caused by this axial filtering implies that cell imaging (typical cell dimensions <15 μm) should not be affected by this suppression of low spatial frequencies. Finally, filtering of the spatial frequency support results in optical sectioning—that is, axial high-pass filtering of the 3D image spectrum. Additionally, the spatial coherence is determined by the illumination aperture and the source spectrum (radius of the coherence area ≈1.36 μm). Objects larger than the coherence area are prone to exhibit smaller phase values[38] (the

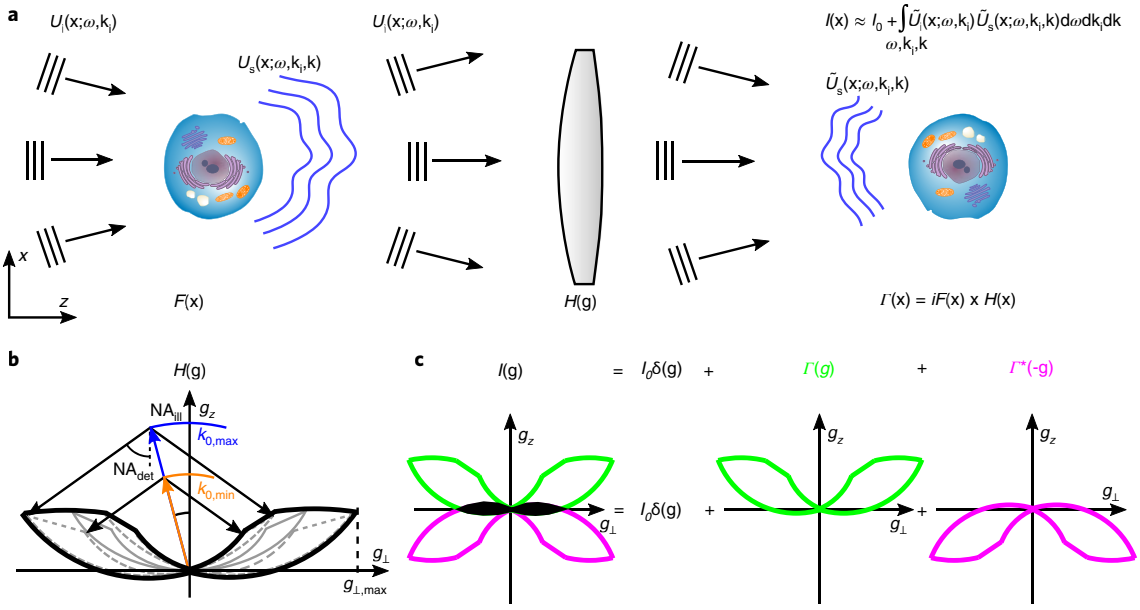

Fig. 1 | Image formation in partial coherent imaging. a, An incident plane wave U_i interacts with a weakly scattering object, that is, its scattering potential F. The scattered field U_s and unscattered field U_i are filtered by the optical system H and their interference is acquired at the image plane. **b**, Polychromatic transfer function H for Koehler illumination based on an Ewald sphere construction. NA, numerical aperture. **c,** Fourier representation of the intensity of the interfering fields at the image plane; Γ cross-spectral density; the spatial frequency overlap is indicated in black. Note: The Ewald sphere is a geometric construct for visualizing elastic light scattering. Therefore, the incident and all scattered wavevectors have the same length.

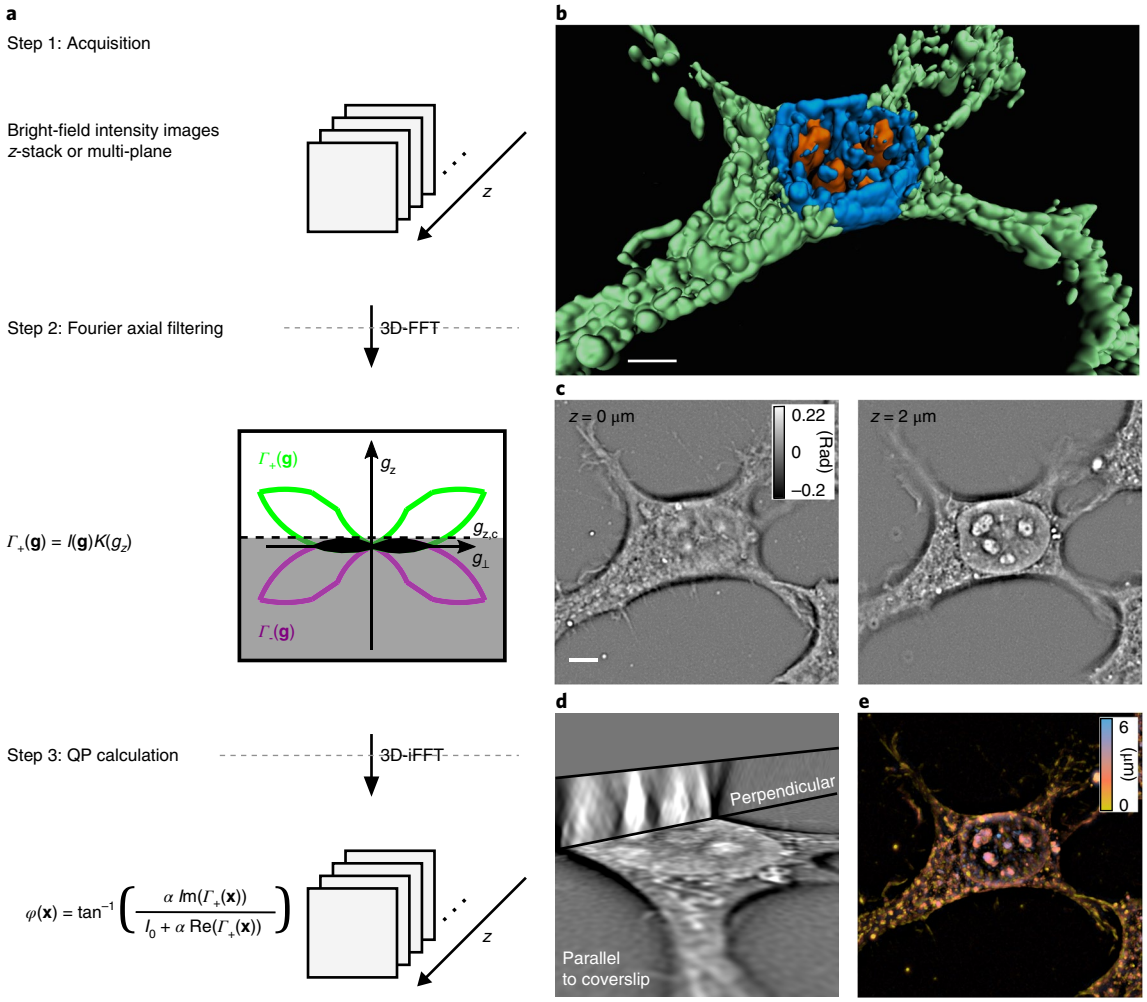

Fig. 2 | White-light cross-spectral density algorithm for 3D phase imaging. a, Algorithm workflow comprising bright-field image stack acquisition, Fourier axial filtering and 3D phase retrieval. **b–e**, 3D quantitative phase imaging using 50 planes acquired with a 20 ms camera exposure time and with an inter-plane spacing of 200 nm. Rendered, false-coloured tomogram (Imaris, Bitplane) of a fixed HeLa cell (**b**) along with selected *xy*-slices (**c**), orthogonal views (**d**) and a colour-coded maximum *z*-projection (**e**) (phase threshold $T=0$). For details see Supplementary Material. Scale bar, 5 µm.

limited spatial coherence causes a lateral high-pass filtering). This is not an issue for our implementation aiming for imaging of fast sub-cellular processes.

After an inverse 3D Fourier transformation, the quantitative phase associated with the image field is retrieved by normalizing the imaginary part of the cross-spectral density as (Supplementary Fig. 2, see Supplementary Section 2)

$$\varphi(\mathbf{x}) = \tan^{-1}\left(\frac{\alpha\ \mathrm{Im}(\Gamma_+(\mathbf{x}))}{I_0 + \alpha\ \mathrm{Re}(\Gamma_+(\mathbf{x}))}\right) \quad (3)$$

The constant α is a calibration factor determined by measuring a technical sample (see Supplementary Section 2.2). We calibrated our method with a staircase-like phase object, characterized using atomic force microscopy. The relative step heights of the nanometric structures are well retrieved. We then validated the phase retrieval by imaging sparsely distributed polystyrene beads embedded in agarose gel. Our experimental data match well the simulated phase point-spread function and amplitude (see Supplementary Section 3, Supplementary Fig. 3). Measurements of beads with different sizes are in excellent agreement with the manufacturer's specification, confirming the quantitativeness of our method (see Supplementary Section 4, Supplementary Fig. 4). The 3D phase recovery is fast and non-iterative as it involves only linear filtering operations. The method requires just $N+1$ intensity images to retrieve the 3D phase information of N planes. The common-path interferometric imaging integrating white-light illumination and high detection $\mathrm{NA}_{\mathrm{det}}$ ($\mathrm{NA}_{\mathrm{det}} = 1.2$) provides high phase sensitivity and high spatial resolution.

Figure 2a summarizes the workflow of our method. The simple algorithm for our forward model results in 3D real time imaging (average processing time of the algorithm optimized for phase accuracy: 0.39 s for a stack of 480 × 480 × 8 pixels on an Intel Xeon E5-2650 v2 @ 2.60 GHz).

We first demonstrate cellular imaging on fixed, well-known HeLa human epithelioid cervix carcinoma cells, as summarized in Fig. 2. The high-resolution 3D phase information was recovered from a *z*-stack of 50 bright-field images acquired with a 20 ms camera exposure time and with a displacement step of 200 nm. In Fig. 2b, the 3D rendered, false-colour-coded tomogram of an adherent cell is shown. The refractive index variations together with the known morphology of subcellular structures allow segmentation of the cellular outline and the cell nucleus containing the high refractive index nucleoli (cell contour in green; nucleus in blue; nucleoli in orange). Selected xy-slices underline the optical sectioning capability and reveal additional intracellular detail (Fig. 2c). Most likely, we observe organelles such as mitochondria and vesicles; even thin

filopodia are clearly visible on the glass substrate. Orthogonal views and a colour-coded maximum z-projection illustrate 3D imaging over a depth of 6 µm (Fig. 2d,e). Additional phase tomograms of a variety of different cell types reveals strikingly different morphologies (HEK 293 T cells, (stimulated) murine macrophages, mouse hippocampal primary neurons and human fibroblast, see Supplementary Fig. 18).

PRISM multi-plane platform. In order to perform fast 3D image acquisition, we conceived a multi-plane platform (MP) based on a novel image splitter. As shown in Fig. 3, a customized image splitting prism in the detection arm of the microscope directs the light into eight distinct images (see Supplementary Section 6, Supplementary Table 1 and Supplementary Figs. 6–9). The image splitter, placed in the convergent beam path, provides high inter-plane image stability for recording a sample volume of about 50 µm x 50 µm x 2.5 µm. The MP platform allows diffraction-limited multiplexed image acquisition of eight planes with no moving parts (optical design provided in Supplementary Sections 6.2 and 6.3, Supplementary Figs. 10–16). The dominant speed limitation is given by the camera frame rate (up to 200 Hz in this work).

Due to the common path configuration and fast 3D (eight-plane) image acquisition, excellent phase stability is achieved. Our high-NA water immersion objective provides a lateral resolution of 380 nm and an axial resolution of 560 nm for phase imaging ($NA_{det} = 1.2$, see Supplementary Section 6, Supplementary Fig. 3). We assessed the influence of the 3D intensity sampling on the phase retrieval in detail. As the prism allows fast imaging of eight planes with an inter-plane distance of 350 nm, we have a trade-off on g_z-sampling in Fourier space. The limited axial sampling translates into an additional lateral and axial high-pass filtering of the phase (see Supplementary Section 5, Supplementary Fig. 5). We have chosen this compromise for the benefit of 3D depth-resolved phase imaging of subcellular structures at 200 Hz.

Due to the classical layout of the microscope, adding an epi-illumination fluorescence channel is straightforward (Fig. 3). The combination of both imaging modalities merges the advantages of phase microscopy, such as label-free, long-term dynamic cell imaging, with the complementary features of fluorescence, for example, molecular specificity and single-molecule detection. We named our multi-plane microscope Phase Retrieval Instrument with Super-resolution Microscopy (PRISM), as wide-field super-resolution imaging can be easily integrated via the fluorescence channel.

PRISM splits the fluorescence signal into eight simultaneously acquired depth images and is ideally suited for 3D Super-resolution Optical Fluctuation Imaging (SOFI). Fast, background-free, super-resolution imaging with inherent optical sectioning is possible by analysing time-series of independent, stochastically blinking emitters with higher-order cumulant statistics[8]. SOFI can be applied on the same dataset as (d)STORM and PALM[11,39]. It also provides reliable results for high labelling densities and limited photon budget, which is an advantage for analysis of the brightness-reduced multi-plane images. Cross-correlation (or precisely cross-cumulant) analysis is not limited to the lateral dimension. In consequence, if the inter-plane distance is adjusted smaller than the axial extent of the point spread funcion and the 3D image stack is acquired simultaneously, a 3D super-resolved image acquisition can be realized (see Supplementary Section 7 and Supplementary Fig. 17). The parallel acquisition significantly reduces the overall imaging time and thus the photobleaching compared to sequential recording of image stacks. We demonstrated a lateral resolution of 110 nm and an axial resolution better than 500 nm for third-order 3D SOFI[10]. The chosen specifications for the new MP configuration allow a robust multiplexed image acquisition matching all these requirements. Using PRISM, we demonstrate high-speed live-cell phase microscopy and the combination of SOFI with phase imaging in 3D.

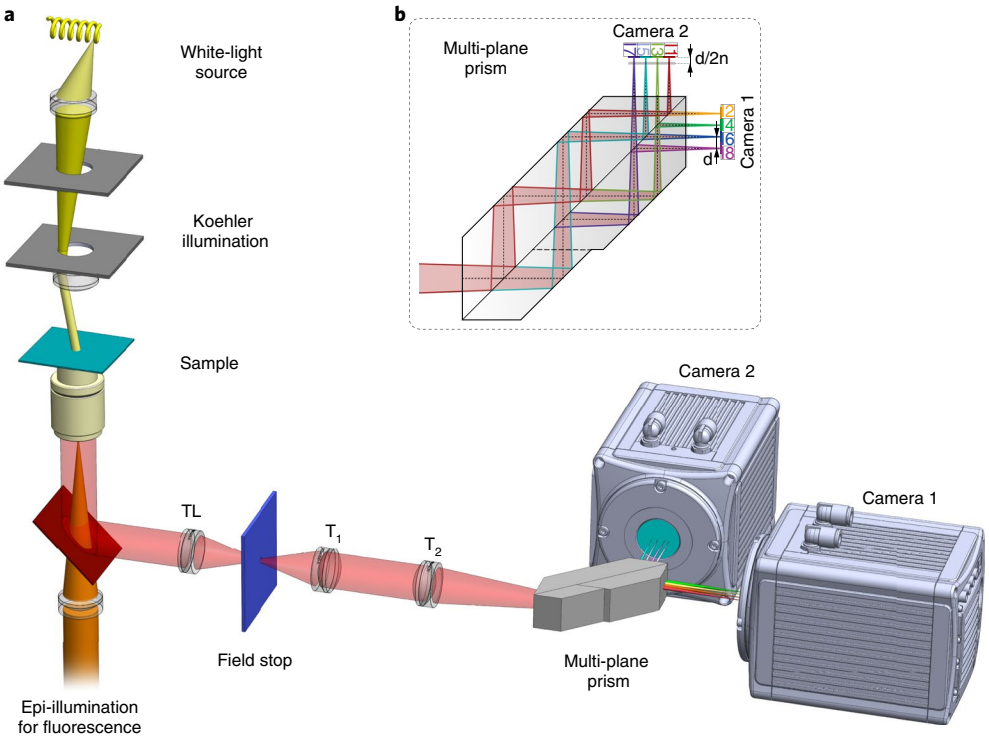

Fig. 3 | Overview of the PRISM set-up. a, Microscope layout combining epi-fluorescence illumination and white-light Koehler illumination for 3D phase retrieval with the multi-plane imaging platform. TL is tube lens, T_1 and T_2 are telescope lenses. **b**, Multi-plane image splitter (for all specifications and parameters see Supplementary Section 6).

High-speed dynamic 3D phase imaging. To highlight the fast acquisition of PRISM 3D phase imaging, we monitored a living human fibroblast at an imaging speed of 200 Hz as it migrates on a glass substrate (see Supplementary Video 1). The overview in Fig. 4a shows the cell body with the nucleus and lamellipodia extending into the direction of migration for a selected plane. The membrane of the nuclear envelope separating the nucleus from the cytoplasm is clearly visible. In the zoomed region of interest (green-dashed square in Fig. 4a), the fast movement of a vesicle (white circle) and an apparent fusion of two small organelles (white arrow) are indicated (Fig. 4b). A kymograph perpendicular to the leading edge of the cell (along the magenta line in Fig. 4a) shows membrane ruffles that move centripetally towards the main body[40] (Fig. 4c). Intracellular vesicle movement in 3D can be observed in the close-up of a colour-coded maximum phase *z*-projection of the green-dashed region of interest (Fig. 4d, the particle that is indicated moves up and down (yellow-red-yellow)). We also performed long-term 3D imaging of a dividing HeLa cell (Supplementary Fig. 19, Supplementary Video 2) undergoing mitosis from metaphase to telophase, highlighting the stability of the phase imaging over an extended period. These experiments demonstrate the performance of our fast and stable label-free multi-plane phase retrieval instrument.

Combining SOFI and phase imaging. We explored the full potential of our PRISM multimodal multi-plane imaging by investigating different cell types using super-resolution optical fluctuation imaging followed by phase imaging, both in 3D (Fig. 5). As a proof of principle, we first acquired image sequences of microtubules in fixed HeLa cells that were fluorescently labelled with Alexa Fluor 647 by indirect immunostaining. We obtained 3D super-resolved images by computing second- and third-order bSOFI[13] images of the fluctuating signals of blinking labels (Fig. 5a).

This SOFI implementation linearizes the brightness response of the cumulants to balance the image contrast (bSOFI)[13]. The optical sectioning capability and the removal of out-of-focus background are apparent in the bSOFI images. A selected xy-plane displays the rich (intra-) cellular context provided by the subsequently acquired corresponding phase tomogram (Fig. 5d). Clearly, the cell nucleus coincides with the void volume that is surrounded by the labelled cytoskeleton filaments, whose network extends almost to the outline of the cell. A colour-coded maximum *z*-projection of the green-dashed region of interest indicated in the 2D phase illustrates the 3D nature of the phase images (Fig. 5g). Our correlative phase and bSOFI images are intrinsically co-aligned, as they were taken successively using the MP microscope without moving the sample.

Figure 5b,e,h summarize the imaging of mouse hippocampal primary neurons that were treated with α-synuclein fibrils. The protein is abundant in the brain and abnormal accumulation of aggregates is a characteristic for a number of neurodegenerative diseases, including Parkinson's[41]. SOFI reveals the 3D architecture of newly formed Alexa Fluor 647-immunostained α-synuclein aggregates (Fig. 5b). Several long fibres extend over the whole imaging depth. The corresponding phase tomogram (Fig. 5e,h) shows that, in this case, most of the α-synuclein aggregates are found within a bundle of neurites. The outline of a neuronal cell body is barely visible slightly off the centre of the 2D image.

Next, we investigated live cells with 3D phase imaging and SOFI. To do so, we transfected RAW 264.7 macrophages with a reversibly photoswitchable fluorescent protein construct, Lifeact-Dreiklang. This fluorescent fusion protein labels actin filaments in live cells[42],

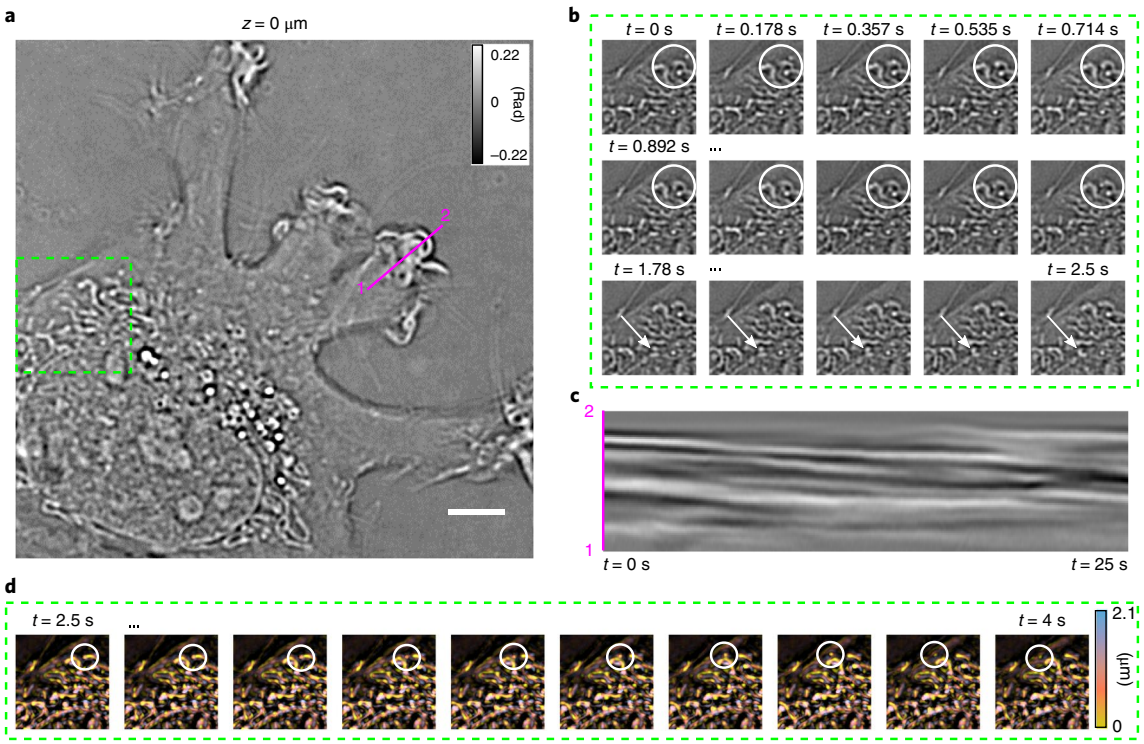

Fig. 4 | Fast live-cell 3D phase imaging of cellular dynamics. a, Human fibroblast migrating on a glass substrate. First frame of a 25 s movie imaged at 200 Hz for a selected plane. **b**, Close-up of the green-dashed ROI indicated in **a** at different times illustrates intracellular organelle movement, indicated by a white circle and a white arrow. **c**, Kymograph for every tenth frame along the magenta line 1–2 in **a** shows ruffling of lamellipodia. **d**, Close-up of the green-dashed ROI indicated in **a** across all planes at different times illustrates intracellular organelle movement in the axial direction, indicated by a white circle. Phase colour-coded maximum *z*-projection (threshold $T = 0$ rad). Scale bar, 5 µm.

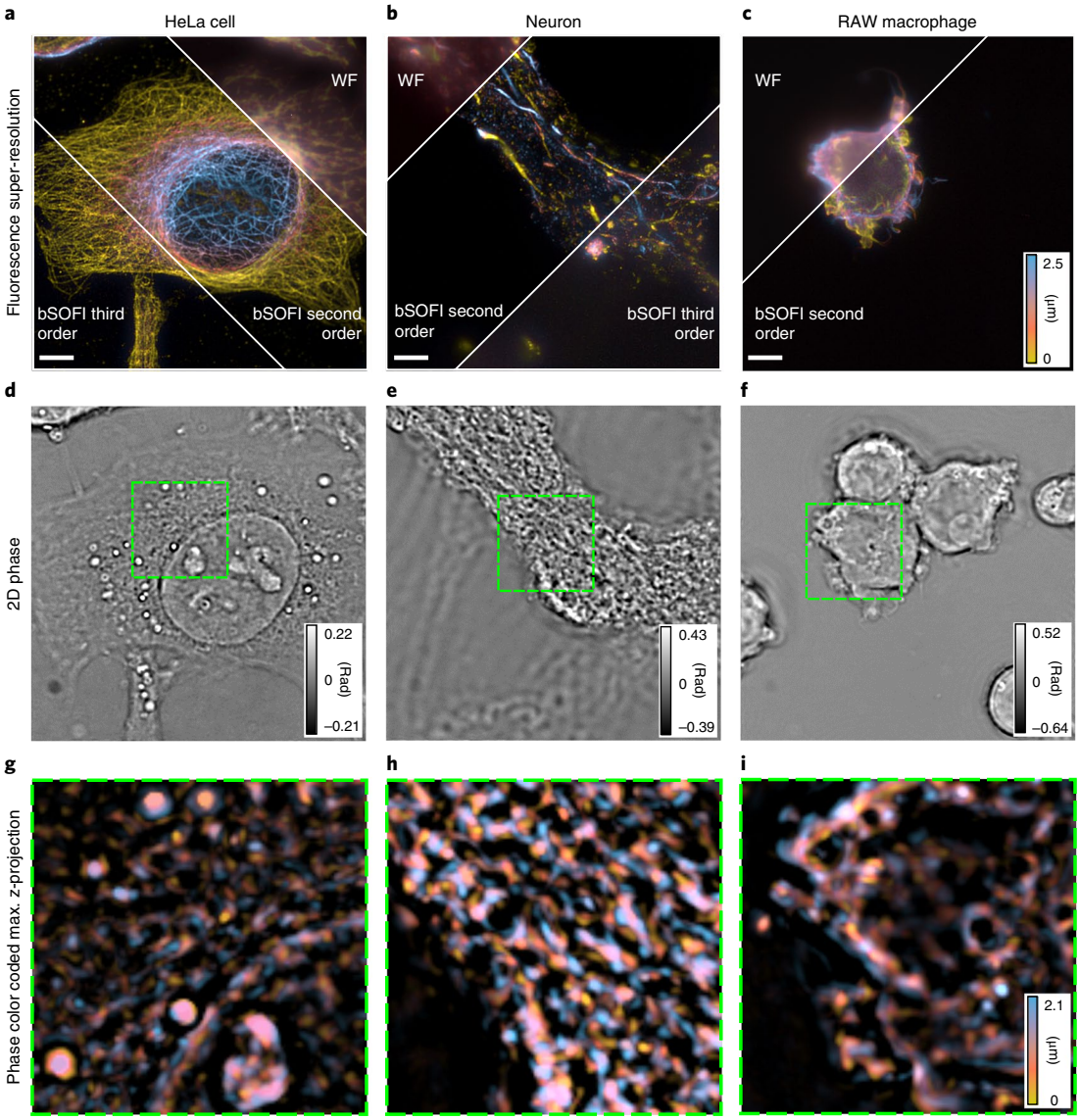

Fig. 5 | Multi-plane SOFI and phase imaging. SOFI maximum intensity projection (**a**,**b**,**c**), selected 2D phase image (**d**,**e**,**f**), and colour-coded maximum phase *z*-projection of the corresponding highlighted area (**g**,**h**,**i**) (threshold $T = 0$ rad). **a**,**d**,**g**, HeLa cell with Alexa Fluor 647 antibody-labelled microtubules. **b**,**e**,**h**, Mouse hippocampal primary neurites incubated with external α-synuclein fibrils and immunostained for newly formed alpha-synuclein aggregates Alexa647. **c**,**f**,**i**, Live murine RAW 264.7 macrophages expressing Lifeact-Dreiklang. SOFI acquisition at 50 Hz of 5,000 frames for Alexa647 and of 3,000 frames for Dreiklang imaging. Subsequent phase imaging camera exposure time 20 ms. Scale bar, 5 μm.

that are visualized in second-order bSOFI (Fig. 5c). A visual comparison between fluorescence and phase imaging reveals that only one out of five cells in the field of view are expressing Lifeact-Dreiklang (Fig. 5c,f). The semi-adherent macrophages have a round shape with several thin, actin-driven protrusions that emerge from the cellular membrane. In addition, we imaged the Vimentin network in HeLa cells and followed their dynamics by longer-term phase imaging (Vimentin-Dreiklang, see Supplementary Fig. 20 and Supplementary Video 3). The diffusion of high-refractive-index vesicles was monitored over 100 s by single-particle tracking, providing an example of analysis of intracellular dynamics.

Summary and discussion. In this study, we provide a novel concept for retrieving the phase information in all three spatial dimensions. The theory is based on the Helmholtz wave equation and is embedded in the framework of the generalized Wiener–Khintchine theorem[35]. We consider elastic light scattering using the first-order Born approximation. An Ewald sphere construction reveals the attainable frequency support of the image spectrum. Measuring the interference of the forward weak scattering with the illumination enables decoding of the phase information along the *z*-direction. The theoretical effort goes in parallel with a fast and elegant algorithm comprising a masking operation to recover the 3D phase information from an acquired volumetric intensity stack. The common-path configuration integrated with white-light Koehler illumination and high detection NA provides stable and speckle-free high-resolution quantitative phase imaging of sub-cellular structures. Our simulations confirmed and matched an experimental lateral and axial resolution of 350 nm and 560 nm. We demonstrated the quantitative nature of our method by assessing the relative step heights of a nanometric phase object, referenced using AFM measurements and confirmed by imaging polystyrene beads of known size. The method allows one to upgrade a classical bright-field microscope into a simple and reliable 3D phase microscope.

The experimental counterpart is based on an innovative multi-plane configuration, containing an image splitting prism for 'volumetric' multiplexing, that is, the simultaneous acquisition of eight images originating from eight conjugated object planes with an inter-plane distance of 350 nm. As shown, the advantage of high-speed 3D image acquisition entails as a compromise the loss of low spatial frequencies. Our Phase Retrieval Instrument with Super-resolution Microscopy (PRISM) combines fast 3D phase imaging with 3D fluorescence super-resolution microscopy for a unique 4D imaging modality.

This powerful and innovative concept opens the door to a wide range of applications, here demonstrated by imaging different cell samples. As shown, retrieving the 3D phase information at an acquisition rate up to 200 Hz responds to an ever growing demand for imaging fast dynamic cell processes. However, the gain in acquisition rate based on phase imaging is paired with a lack of specificity. Since our proposed MP configuration allows super-resolved fluorescence imaging based on super-resolution optical fluctuation imaging, fluorescence-based specificity and high acquisition speed are realized in the same 3D platform. This multimodal and versatile microscope promises to fulfil the expectations for many novel applications and investigations in biology and the life sciences.

Methods

Methods, including statements of data availability and any associated accession codes and references, are available at https://doi.org/10.1038/s41566-018-0109-4.

Received: 16 May 2017; Accepted: 22 January 2018;
Published online: 26 February 2018

References

1. Rust, M. J., Bates, M. & Zhuang, X. W. Sub-diffraction-limit imaging by stochastic optical reconstruction microscopy (STORM). *Nat. Methods* **3**, 793–796 (2006).
2. Heilemann, M. et al. Subdiffraction-resolution fluorescence imaging with conventional fluorescent probes. *Angew. Chem. Int. Ed.* **47**, 6172–6176 (2008).
3. Betzig, E. et al. Imaging intracellular fluorescent proteins at nanometer resolution. *Science* **313**, 1642–1645 (2006).
4. Vandenberg, W., Leutenegger, M., Lasser, T., Hofkens, J. & Dedecker, P. Diffraction-unlimited imaging: from pretty pictures to hard numbers. *Cell Tissue Res.* **360**, 151–178 (2015).
5. Tinnefeld, P., Eggeling, C. & Hell, S. W. *Far-Field Optical Nanoscopy* (Springer, 2015).
6. Small, A. R. & Parthasarathy, R. Superresolution localization methods. *Annu. Rev. Phys. Chem.* **65**, 107–125 (2014).
7. Liu, Z., Lavis, L. D. & Betzig, E. Imaging live-cell dynamics and structure at the single-molecule level. *Mol. Cell* **58**, 644–659 (2015).
8. Dertinger, T., Colyer, R., Iyer, G., Weiss, S. & Enderlein, J. Fast, background-free, 3D super-resolution optical fluctuation imaging (SOFI). *Proc. Natl Acad. Sci. USA* **106**, 22287–22292 (2009).
9. Dertinger, T., Xu, J., Naini, O. F., Vogel, R. & Weiss, S. SOFI-based 3D superresolution sectioning with a widefield microscope. *Opt. Nanoscopy* **1**, 2–5 (2012).
10. Geissbuehler, S. et al. Live-cell multiplane three-dimensional super-resolution optical fluctuation imaging. *Nat. Commun.* **5**, 5830 (2014).
11. Geissbuehler, S., Dellagiacoma, C. & Lasser, T. Comparison between SOFI and STORM. *Biomed. Opt. Express* **2**, 408–420 (2011).
12. Girsault, A. et al. SOFI simulation tool: a software package for simulating and testing super-resolution optical fluctuation imaging. *PLoS One* **11**, e0161602 (2016).
13. Geissbuehler, S. et al. Mapping molecular statistics with balanced super-resolution optical fluctuation imaging (bSOFI). *Opt. Nanoscopy* **1**, 4 (2012).
14. Lukeš, T. et al. Quantifying protein densities on cell membranes using super-resolution optical fluctuation imaging. *Nat. Commun.* **8**, 1731 (2017).
15. Liebling, M. Imaging the dynamics of biological processes via fast confocal microscopy and image processing. *Cold Spring Harb. Protoc.* **6**, 783–789 (2011).
16. Grewe, B. F., Langer, D., Kasper, H., Kampa, B. M. & Helmchen, F. High-speed in vivo calcium imaging reveals neuronal network activity with near-millisecond precision. *Nat. Methods* **7**, 399–405 (2010).
17. Chen, B.-C. et al. Lattice light-sheet microscopy: Imaging molecules to embryos at high spatiotemporal resolution. *Science* **346**, 1257998 (2014).
18. Wolf, E. Three-dimensional structure determination of semi-transparent objects from holographic data. *Opt. Commun.* **1**, 153–156 (1969).
19. Mir, M., Bhaduri, B., Wang, R., Zhu, R. & Popescu, G. Quantitative phase imaging. *Prog. Opt.* **57**, 133–217 (2012).
20. Gabor, D. A New microscopic principle. *Nature* **161**, 777–778 (1948).
21. Goodman, J. W. & Lawrence, R. W. Digital image formation from electronically detected holograms. *Appl. Phys. Lett.* **11**, 77–79 (1967).
22. Cuche, E., Bevilacqua, F. & Depeursinge, C. Digital holography for quantitative phase-contrast imaging. *Opt. Lett.* **24**, 291–293 (1999).
23. Ikeda, T., Popescu, G., Dasari, R. R. & Feld, M. S. Hilbert phase microscopy for investigating fast dynamics in transparent systems. *Opt. Lett.* **30**, 1165–1167 (2005).
24. Popescu, G. et al. Fourier phase microscopy for investigation of biological structures and dynamics. *Opt. Lett.* **29**, 2503–2505 (2004).
25. Wang, Z. et al. Spatial light interference microscopy (SLIM). *Opt. Express* **19**, 1016–1026 (2011).
26. Reed Teague, M. Deterministic phase retrieval: a Green's function solution. *J. Opt. Soc. Am.* **73**, 1434–1441 (1983).
27. Streibl, N. Phase imaging by the transport equation of intensity. *Opt. Commun.* **49**, 6–10 (1984).
28. Kou, S. S., Waller, L., Barbastathis, G. & Sheppard, C. J. R. Transport-of-intensity approach to differential interference contrast (TI-DIC) microscopy for quantitative phase imaging. *Opt. Lett.* **35**, 447–449 (2010).
29. Bostan, E., Froustey, E., Nilchian, M., Sage, D. & Unser, M. Variational phase imaging using the transport-of-intensity equation. *IEEE Trans. Image Process.* **25**, 807–817 (2015).
30. Kim, T. et al. White-light diffraction tomography of unlabelled live cells. *Nat. Photon.* **8**, 256–263 (2014).
31. Chen, M., Tian, L. & Waller, L. 3D differential phase contrast microscopy. *Biomed. Opt. Express* **7**, 3940–3950 (2016).
32. Chowdhury, S., Eldridge, W. J., Wax, A. & Izatt, J. A. Structured illumination multimodal 3D-resolved quantitative phase and fluorescence sub-diffraction microscopy. *Biomed. Opt. Express* **8**, 2496–2518 (2017).
33. Choi, W. et al. Tomographic phase microscopy. *Nat. Methods* **4**, 717–719 (2007).
34. Born, M. & Wolf, E. *Principles of Optics,* 7th (expanded) ed. (Cambridge Univ. Press, Cambridge, UK, 1999).
35. Mandel, L. & Wolf, E. *Optical Coherence and Quantum Optics* (Cambridge Univ. Press, Cambridge, UK, 1995).
36. McCutchen, C. W. Generalized aperture and the three-dimensional diffraction image. *J. Opt. Soc. Am. A* **54**, 240–244 (1964).
37. Sheppard, C. J. R., Gu, M., Kawata, Y. & Kawata, S. Three-dimensional transfer functions for high-aperture systems. *J. Opt. Soc. Am. A* **11**, 593–598 (1994).
38. Edwards, C. et al. Effects of spatial coherence in diffraction phase microscopy. *Opt. Express* **22**, 5133–5146 (2014).
39. Deschout, H. et al. Complementarity of PALM and SOFI for super-resolution live-cell imaging of focal adhesions. *Nat. Commun.* **7**, 13693 (2016).
40. Borm, B., Requardt, R. P., Herzog, V. & Kirfel, G. Membrane ruffles in cell migration: Indicators of inefficient lamellipodia adhesion and compartments of actin filament reorganization. *Exp. Cell Res.* **302**, 83–95 (2005).
41. Lashuel, H. A., Overk, C. R., Oueslati, A. & Masliah, E. The many faces of α-synuclein: from structure and toxicity to therapeutic target. *Nat. Rev. Neurosci.* **14**, 38–48 (2013).
42. Riedl, J. et al. Lifeact: a versatile marker to visualize F-actin. *Nat. Methods* **5**, 605–607 (2008).

Acknowledgements

We thank P. Sandoz and G. van der Goot for construction of Lifeact-Dreiklang (VDG-EPFL), the LSBG-EPFL for providing RAW 264.7 cells and M. Ricchetti from Institute Pasteur for human fibroblast cells. We are grateful to M. Sison for cell culture advice and assistance. We thank O. Peric and G. Fantner (LBNI-EPFL) for providing the technical sample and performing the AFM measurement. We acknowledge A. Radenovic and A. Nahas for support and discussion and G. M. Hagen for proofreading of the manuscript. This project has been partly funded from the European Union's Horizon 2020 research and innovation program under the Marie Skłodowska-Curie Grant Agreement No. [750528]. The research was supported by the Swiss National Science Foundation (SNSF) under grant 200020_159945/1. T.L. acknowledges the support from the Horizon 2020 Framework Programme of the European Union via grant 686271.

Author contributions

A.D. and K.S.G. contributed equally to this work. T.L. and A.D. initiated the project and wrote the theory/modelling. A.D. developed the phase retrieval algorithm and simulations. K.S.G., A.D., T.L. and A.S. designed the experiments. K.S.G. prepared and

performed the experiments. A.-L. M.-M. prepared the neuron samples. A.D., K.S.G. and T.Lu. analysed the data. M.L., S.G. and T.L. designed the optical system including the image splitting prism. S.G. and A.S. built the microscope set-up. E.B., A.B. and H.A.L. provided research advice. A.D., K.S.G. and T.L. wrote the manuscript with contributions from all authors.

Competing interests

The authors declare no competing interests.

Additional information

Supplementary information is available for this paper at https://doi.org/10.1038/s41566-018-0109-4.

Reprints and permissions information is available at www.nature.com/reprints.

Correspondence and requests for materials should be addressed to T.L.

Publisher's note: Springer Nature remains neutral with regard to jurisdictional claims in published maps and institutional affiliations.

Methods

Microscope set-up. All imaging was performed with a custom-built microscope equipped with a temperature and CO_2 controlled incubator for live cell imaging[10]. For phase imaging we used a white-light Koehler illumination module. This optical system corresponds to a classical wide-field set-up with an integrated low-magnification telescope (see Fig. 3 and Supplementary Section 6).

For fluorescence imaging, a 120 mW, 405 nm laser (iBeam smart, Toptica), an 800 mW, 635 nm laser (MLL-III-635, Roithner Lasertechnik), and an 800 mW, 532 nm laser (MLL-FN-532, Roithner Lasertechnik) were combined and focused into the back focal plane of an Olympus UPLSAPO 60XW 1.2 NA objective for wide-field epi-fluorescence illumination. The fluorescence light was filtered using a combination of a dichroic mirror (zt405/488/532/640/730rpc, Chroma) and an emission filter adapted to the respective experiment (see Supplementary Table 2).

For phase imaging, we used the Koehler illumination module of a Zeiss Axiovert 100 M microscope equipped with a halogen lamp (for spectrum, see Supplementary Fig. 8). The detection path is arranged as a sequence of four 2-f configurations to provide image–object space telecentricity. The image splitter placed behind the last lens directs the light into eight images, which are registered by two synchronized sCMOS cameras (ORCA Flash 4.0, Hamamatsu; back projected pixel size of 111 nm). For translating the sample, the microscope is equipped with piezoLEGS stage (3-PT-60- F2,5/5) and Motion-Commander-Piezo controller (Nanos Instruments GmbH).

A more detailed description of the set-up is given in the Supplementary Section 6 and Supplementary Table 1.

Cell culture. HeLa cells, HEK293T cells, human fibroblasts and RAW 264.7 cells were cultured at 37 °C and 5% CO_2 using DMEM high glucose with pyruvate (4.5 g l^{-1} glucose, with GlutaMAX supplement, Gibco, Thermo Fisher Scientific or Roti-CELL DMEM, Roth) supplemented with 10% foetal bovine serum and 1 × penicillin-streptomycin (both Gibco, Thermo Fisher Scientific).

RAW 264.7 stimulation. RAW 264.7 cells were stimulated with 100 ng ml^{-1} lipopolysaccharides from *Escherichia coli* O111:B4 in DMEM (see Cell culture) for about 4 h at 37 °C and 5% CO_2.

Cell fixation for phase and fluorescence imaging. Cells were seeded in Lab-tek II chambered cover slides (nunc) or in FluoroDish Sterile Culture Dish 35 mm, 23 mm well (World Precision Instruments) one to two days before fixation in DMEM (see Cell culture) or DMEM high glucose without phenol red (4.5 g l^{-1} glucose) supplemented with 4 mM L-gluthamine, 10% foetal bovine serum and 1× penicillin-streptomycin (all gibco, Thermo Fisher Scientific).

Cells were washed twice in pre-warmed microtubule stabilizing buffer (MTSB: 100 mM PIPES pH 6.8, 2 mM $MgCl_2$, 5 mM EGTA), followed by application of pre-warmed fixation buffer (MTSB with 3.7% paraformaldehyde (PFA) and 0.2% Triton X-100 for microtubule immunostaining) for 15 min at room temperature (RT). Cells were then washed three times for 5 min each with 1 × PBS and stored in 50% glycerol in 1 × PBS at 4 °C until phase imaging, or the immunostaining protocol was continued to prepare samples for fluorescence imaging.

Immunostaining HeLa cells. Fixed and permeabilized cells were blocked with 3% BSA in 1 × PBS and 0.05% Triton X-100 for 60 min at RT or overnight at 4 °C. The blocked samples were immediately incubated with primary anti-tubulin antibody (0.01 mg ml^{-1} DM1A mouse monoclonal, Abcam) in antibody incubation buffer for 60 min at RT (AIB: 1% BSA in 1 × PBS and 0.05% Triton X-100). Cells were then washed three times for 5 min each with AIB, followed by incubation with donkey anti-mouse-Alexa Fluor 647 antibody (0.01 mg ml^{-1} Invitrogen) for 60 min at RT. All subsequent steps were performed in the dark. Cells were again washed three times for 5 min each with AIB, incubated for 15 min post-fixation with 2% PFA in 1 × PBS, followed by three 5 min washes with PBS. Cells were imaged immediately, or stored in 50% glycerol in 1 × PBS at 4 °C until imaging.

Transfection and plasmid construction. Cells were transfected using FuGENE 6 transfection reagent (Promega) at about 80% confluence in FluoroDish Sterile Culture Dishes 35 mm, 23 mm well (World Precision Instruments) according to the manufacturer's protocols. For each dish with HeLa cells, 6 µl FuGENE 6 were mixed with 92 µl OptiMEM Reduced-Serum Medium (Life Technologies) and incubated for 5 min before the addition of 2 ng of the plasmid pMD-Vim-Dreiklang[43]. For each dish with RAW 264.7 cells, 9.6 µl FuGENE® 6 were mixed with 125.2 µl OptiMEM Reduced-Serum Medium (Life Technologies) and incubated for 5 min before the addition of 2.8 ng of the plasmid pCDNA3-Lifeact-Dreiklang. After incubation for 30 min at RT, 100 µl and 125 µl of the solution was carefully distributed over the cells that were supplied with fresh medium, respectively. Cells were then returned to the incubator and left overnight before imaging.

Lifeact-Dreiklang was constructed as follows: the Dreiklang sequence (Aberrior) was amplified by PCR and inserted in the plasmid pCDNA3 (Invitrogen) using PmeI and AgeI restriction sites. The Lifeact sequence was synthesized (Microsynth) according to Riedl et al.[42], annealed and inserted in front of Dreiklang using KpnI and BstBI restriction sites.

Primary neuron culture preparation. Pregnant female C57BL/6 J Rcc Hsd were obtained from Harlan Laboratories (France) and were housed according to the Swiss legislation and the European Community Council directive (86/609/EEC). Primary hippocampal cultures were prepared from mice brains from P0 pups as previously described[44]. The protocol was approved by the Swiss cantonal authorities VD, 'Service de la consommation et des affaires vétérinaires' Lausanne, Switzerland. Briefly, the hippocampi were isolated stereoscopically and dissociated by trituration in medium containing papain (20 U ml^{-1}, Sigma-Aldrich, Switzerland). The neurons were plated on FluoroDish Sterile Culture Dish 35 mm, 23 mm well (World Precision Instruments), previously coated with poly-L-lysine 0.1% w/v in water, and neurons were cultured in Neurobasal medium containing B27 supplement (Life Technologies), L-glutamine and penicillin/streptomycin (100 U ml^{-1}, Life Technologies).

Treatment of hippocampal neurons with α-synuclein (α-syn) pre-formed fibrils. After five days in vitro, the hippocampal neurons were treated with α-syn pre-formed fibrils (PFFs) prepared and characterized as previously described[45]. Briefly, α-syn PFFs were diluted in the neuronal cell culture media at a final concentration of 70 nM and added to the hippocampal neurons for ten days as described by Lee's group[46,47]. The extracellular α-syn PFFs, once internalized by the hippocampal primary neurons, recruit endogenous α-syn, which leads to the formation of new intracellular aggregates hyperphosphorylated on the S129 residue of α-syn. These newly formed aggregates can be detected by immunocytochemistry ten days post-treatment using an antibody that specifically stains α-syn phosphorylated on S129 (pS129)[46,47].

Staining of neurons. The hippocampal primary neurons were washed twice with PBS (Life Technologies) and were then fixed in 4% paraformaldehyde for 20 minutes at RT. After two washings in PBS, neurons were incubated in 3% bovine serum albumin (BSA) in 0.1% Triton X-100 PBS (PBS-T) for 30 min at RT. Hippocampal primary neurons were then incubated with primary antibodies [chicken anti-MAP2 (Abcam) to specifically stain the neurons, mouse anti-α-syn (SYN-1, BD) to detect the total level of α-syn and rabbit anti-pS129-α-syn (MJFR-13, Abcam) to detect the newly formed aggregates] for 2 hours at RT. The cells were rinsed five times in PBS-T and subsequently incubated respectively with the secondary donkey anti-chicken Alexa488 (Jackson ImmunoResearch), anti-mouse Alexa594 and anti-rabbit Alexa647 (Life Technologies) at a dilution of 1/800 in PBS-T and DAPI at 2 µg ml^{-1} (Life Technologies). The cells were washed five times in PBS-T and twice in PBS before being imaged.

Imaging media/buffer. Phase imaging of fixed samples was performed in 1 × PBS. The Alexa647 immunostained samples for SOFI were imaged in a 50 mM Tris-HCl pH 8.0, 10 mM NaCl buffer containing an enzymatic oxygen scavenging system (2.5 mM protocatechuic acid (PCA) and 50 nM Protocatechuate-3,4-Dioxygenase from Pseudomonas Sp. (PCD) with >3 Units mg^{-1})[48] and a thiol (2-Mercaptoethylamine). The thiol and a stock solution of 100 mM PCA in water, pH adjusted to 9.0 with NaOH, were prepared on the measurement day and PCD was aliquoted at a concentration of 10 µM in storage buffer (100 mM Tris-HCl pH 8.0, 50% glycerol, 50 mM KCl, 1 mM EDTA) at −20 °C.

Live cell imaging. Label-free imaging was performed in DMEM or DMEM without phenol red at 35 °C and 5% CO_2 (for details, see Cell culture). For living cells with Dreiklang plasmids, the medium was exchanged to antibleaching medium DMEM^{gfp}-2 supplemented with rutin (Evrogen) at a final concentration of 20 mg l^{-1} approximately 15–30 min before imaging.

Chemicals. Unless noted otherwise, all chemicals were purchased at Sigma-Aldrich.

Signal processing and rendering. All data processing was done using Matlab (Mathworks). All 3D rendering was performed using Imaris (Bitplane). All other images were rendered using ImageJ[49].

Life Sciences Reporting Summary. Further information on experimental design is available in the Life Sciences Reporting Summary.

Code availability. All customized code will be made available upon request by the corresponding author.

Data availability. The data that support the plots within this paper and other findings of this study are available from the corresponding author upon reasonable request.

References

43. Brakemann, T. et al. A reversibly photoswitchable GFP-like protein with fluorescence excitation decoupled from switching. *Nat. Biotechnol.* **29**, 942–947 (2011).

44. Steiner, P. et al. Modulation of receptor cycling by neuron-enriched endosomal protein of 21 kD. *J. Cell Biol.* **157**, 1197–1209 (2002).
45. Mahul-Mellier, A.-L. et al. Fibril growth and seeding capacity play key roles in α-synuclein-mediated apoptotic cell death. *Cell Death Differ.* **22**, 1–16 (2015).
46. Volpicelli-Daley, L. A., Luk, K. C. & Lee, V. M.-Y. Addition of exogenous α -synuclein preformed fibrils to primary neuronal cultures to seed recruitment of endogenous α-synuclein to Lewy body and Lewy neurite-like aggregates. *Nat. Protoc.* **9**, 2135–2146 (2014).
47. Volpicelli-Daley, L. A. et al. Exogenous α-synuclein fibrils induce Lewy body pathology leading to synaptic dysfunction and neuron death. *Neuron* **72**, 57–71 (2011).
48. Aitken, C. E., Marshall, R. A. & Puglisi, J. D. An oxygen scavenging system for improvement of dye stability in single-molecule fluorescence experiments. *Biophys. J.* **94**, 1826–1835 (2008).
49. Abràmoff, M. D., Magalhães, P. J. & Ram, S. J. Image processing with ImageJ. *Biophotonics International* **11**, 36–42 (2004).

nature research

Corresponding author(s): Prof. Theo Lasser

Life Sciences Reporting Summary

Nature Research wishes to improve the reproducibility of the work that we publish. This form is intended for publication with all accepted life science papers and provides structure for consistency and transparency in reporting. Every life science submission will use this form; some list items might not apply to an individual manuscript, but all fields must be completed for clarity.

For further information on the points included in this form, see Reporting Life Sciences Research. For further information on Nature Research policies, including our data availability policy, see Authors & Referees and the Editorial Policy Checklist.

Please do not complete any field with "not applicable" or n/a. Refer to the help text for what text to use if an item is not relevant to your study.
For final submission: please carefully check your responses for accuracy; you will not be able to make changes later.

Experimental design

1. Sample size

   Describe how sample size was determined. — All imaging has been done on single cells.

2. Data exclusions

   Describe any data exclusions. — Cells have been selected visually according to staining quality.

3. Replication

   Describe the measures taken to verify the reproducibility of the experimental findings. — We repeated several single cell imaging (>10 typically) for ensuring the reproducibility of the experimental findings.

4. Randomization

   Describe how samples/organisms/participants were allocated into experimental groups. — This is not applicable for single cell imaging.

5. Blinding

   Describe whether the investigators were blinded to group allocation during data collection and/or analysis. — This is not applicable for single cell imaging.

Note: all in vivo studies must report how sample size was determined and whether blinding and randomization were used.

6. Statistical parameters

   For all figures and tables that use statistical methods, confirm that the following items are present in relevant figure legends (or in the Methods section if additional space is needed).

n/a	Confirmed
☐	☒ The exact sample size (*n*) for each experimental group/condition, given as a discrete number and unit of measurement (animals, litters, cultures, etc.)
☐	☒ A description of how samples were collected, noting whether measurements were taken from distinct samples or whether the same sample was measured repeatedly
☒	☐ A statement indicating how many times each experiment was replicated
☒	☐ The statistical test(s) used and whether they are one- or two-sided *Only common tests should be described solely by name; describe more complex techniques in the Methods section.*
☒	☐ A description of any assumptions or corrections, such as an adjustment for multiple comparisons
☒	☐ Test values indicating whether an effect is present *Provide confidence intervals or give results of significance tests (e.g. P values) as exact values whenever appropriate and with effect sizes noted.*
☐	☒ A clear description of statistics including central tendency (e.g. median, mean) and variation (e.g. standard deviation, interquartile range)
☒	☐ Clearly defined error bars in all relevant figure captions (with explicit mention of central tendency and variation)

See the web collection on statistics for biologists for further resources and guidance.

Software

Policy information about availability of computer code

7. Software

Describe the software used to analyze the data in this study.	We used Image J 1.51k, Matlab 2015a, 2017b (Mathworks) and Imaris (Bitplane). Custom algorithms for quantitative phase reconstruction and for 3D bSOFI analysis were implemented in Matlab (see Supplementary Material for description).

For manuscripts utilizing custom algorithms or software that are central to the paper but not yet described in the published literature, software must be made available to editors and reviewers upon request. We strongly encourage code deposition in a community repository (e.g. GitHub). *Nature Methods* guidance for providing algorithms and software for publication provides further information on this topic.

Materials and reagents

Policy information about availability of materials

8. Materials availability

Indicate whether there are restrictions on availability of unique materials or if these materials are only available for distribution by a third party.	All unique materials are readily available upon request from the authors or from commercial source.

9. Antibodies

Describe the antibodies used and how they were validated for use in the system under study (i.e. assay and species).	anti alpha-tubulin DM1a mouse monoclonal, (ref ab7291, Abcam, validated by Abcam), anti-pS129-α-syn rabbit (ref ab168381, clone MJFR-13, Abcam) anti-α-syn mouse (ref 610787, clone SYN-1, BD) anti-MAP2 chicken (ref ab92434, Abcam) anti-donkey anti-mouse IgG (H+L) highly cross-adsorbed secondary antibody, Alexa 647 Fluor (A-31571, Invitrogen, validated by Invitrogen). donkey anti-rabbit Alexa647 IgG (H+L) highly cross-adsorbed secondary antibody(A-31573, Invitrogen, validated by Invitrogen) donkey anti-mouse Alexa568 IgG (H+L) highly cross-adsorbed secondary antibody(A10037, Invitrogen, validated by Invitrogen) Alexa Fluor® 488 AffiniPure Donkey Anti-Chicken IgY (IgG) (H+L) (Jackson ImmunoResearch)

10. Eukaryotic cell lines

a. State the source of each eukaryotic cell line used.	RAW 264.7 cells were a gift from the lab of B. Deplancke (LSBG-EPFL), fibroblast cells were a gift from M. Ricchetti from Institute Pasteur, HeLa cells were obtained from ATCC, and HEK293T cells were a gift from the lab of A. Radenovic (LBEN-EPFL).
b. Describe the method of cell line authentication used.	We did not perform authentication of the cell lines.
c. Report whether the cell lines were tested for mycoplasma contamination.	Cell lines were not tested for mycoplasma contamination.
d. If any of the cell lines used are listed in the database of commonly misidentified cell lines maintained by ICLAC, provide a scientific rationale for their use.	No commonly misidentified cell lines were used.

Animals and human research participants

Policy information about studies involving animals; when reporting animal research, follow the ARRIVE guidelines

11. Description of research animals

Provide all relevant details on animals and/or animal-derived materials used in the study.	Pregnant female C57BL/6J Rcc Hsd were obtained from Harlan Laboratories (France) and were housed according to the Swiss legislation and the European Community Council directive (86/609/EEC). Primary hippocampal cultures were prepared from mice brains from P0 pups as described previously (see Methods section)

Policy information about studies involving human research participants

12. Description of human research participants

Describe the covariate-relevant population characteristics of the human research participants.	The study did not involve human participants.